Contract No:

This document was prepared in conjunction with work accomplished under Contract No. DE-AC09-08SR22470 with the U.S. Department of Energy (DOE) Office of Environmental Management (EM).

Disclaimer:

We put science to work.™

Savannah River National Laboratory®

OPERATED BY SAVANNAH RIVER NUCLEAR SOLUTIONS

A U.S. DEPARTMENT OF ENERGY NATIONAL LABORATORY • SAVANNAH RIVER SITE • AIKEN, SC

Simulations of Crack Extensions in Arc-Shaped Specimens of Uncharged and Tritium-Charged-and-Decayed Austenitic Stainless Steels Using Cohesive Zone Modeling

Prepared for publication in the Proceedings of the ASME 2020 Pressure Vessel and Piping Conference, PVP2020, July 19-24, 2020, Minneapolis, Minnesota, USA, PVP2020-21308

Jwo Pan[1], Shin-Jang Sung[1], Shengjia Wu[1], Michael Morgan[2], & Paul Korinko[2]

[1]University of Michigan, [2]Savannah River National Laboratory

March 2020

SRNL-STI-2020-00103

Proceedings of the ASME 2020
Pressure Vessels and Piping Conference
PVP2020
July 19-24, 2020, Minneapolis, Minnesota, USA

PVP2020-21737

SIMULATIONS OF CRACK EXTENSIONS IN ARC-SHAPED TENSION SPECIMENS OF UNCHARGED AND TRITIUM-CHARGED-AND-DECAYED AUSTENITIC STAINLESS STEELS USING COHESIVE ZONE MODELING

Shengjia Wu, Jwo Pan
Department of Mechanical Engineering
University of Michigan
Ann Arbor, Michigan, USA

Paul S. Korinko, Michael J. Morgan
Materials Science and Technology
Savannah River National Laboratory
Aiken, South Carolina, USA

ABSTRACT

Crack extensions in arc-shaped tension specimens of uncharged and tritium-charged-and-decayed conventionally forged (CF) 21-6-9 austenitic stainless steels are simulated by two-dimensional finite element analyses using the cohesive zone modeling (CZM) approach with the smooth trapezoidal traction-separation law. The J integrals at the deviation loads of the arc-shaped tension specimens are taken as the reference cohesive energies and the maximum opening stresses ahead of the initial crack tips in the arc-shaped tension specimens are taken as the reference cohesive strengths. The cohesive strengths and cohesive energies are then adjusted to match the maximum loads of the experimental load-displacement curves of the arc-shaped tension specimens. The computational results showed that the computational load-displacement, load-crack extension, crack extension-displacement, and J-R curves of the uncharged and tritium-charged-and-decayed CF steel specimens are compared well with the experimental data.

1. INTRODUCTION

Austenitic stainless steels are used for containment vessels for hydrogen and its isotopes [1, 2]. Uniaxial tension tests were conducted to obtain the stress-strain curves of uncharged, hydrogen-charged, and tritium-charged-and-decayed high-energy-rate-forged (HERF) 21-6-9 stainless steels [1]. The test results in Morgan [1] showed that while the hydrogen-charged and tritium-charged-and-decayed HERF 21-6-9 stainless steels have higher strengths and lower ductility than those of the uncharged HERF 21-6-9 stainless steels, the hydrogen-charged and tritium-charged-and-decayed HERF 21-6-9 stainless steels still failed in a ductile manner dominated by void nucleation and growth process. Fracture tests were also conducted to obtain the J-R curves of uncharged, hydrogen-charged, and tritium-charged-and-decayed conventionally forged (CF) 21-6-9 stainless steel specimens and high-energy-rate-forged (HERF) 21-6-9 stainless steel specimens [2]. The test results in Morgan [2] indicated that the hydrogen-charged and tritium-charged-and-decayed specimens have lower J-R curves than those of the uncharged specimens. The J-R curve of the tritium-charged-and-decayed specimen is significantly lower than that of the uncharged specimen. The test results in Morgan [2] also showed the fracture surfaces of the hydrogen-charged and tritium-charged-and-decayed specimens are still dominated by void nucleation and growth process. The fracture test data of the uncharged and tritium-charged-and-decayed CF 21-6-9 austenitic stainless steel specimens in Morgan [2] are analyzed in this investigation to examine the applicability of the cohesive zone model to simulate the experimental load-displacement-crack extension data.

In this paper, the material constitutive relation for the uncharged CF steel reported in [3] is adopted. The material constitutive relation for the tritium-charged-and-decayed CF steel is estimated based on the experimental tensile stress-strain data of the uncharged CF steel and the tritium-charged-and-decayed HERF 21-6-9 stainless steel. The cohesive zone model with the smooth trapezoidal traction-separation law is then adopted to simulate crack extensions in arc-shaped tension specimens of the uncharged and tritium-charged-and-decayed CF steels. The J integrals at the deviation loads of the arc-shaped tension specimens are taken as the reference cohesive energies and the maximum opening stresses ahead of the initial crack tips in the arc-shaped tension specimens are taken as the

This document was prepared in conjunction with work accomplished under Contract No. DE-AC09-08SR22470 with the U.S. Department of Energy.

reference cohesive strengths for the uncharged and tritium-charged-and-decayed CF steel specimens. The cohesive strengths and cohesive energies are then adjusted to match the maximum loads of the experimental load-displacement curves of the arc-shaped tension specimens. The computational load-displacement, load-crack extension and crack extension-displacement, and J-R curves for the uncharged and tritium-charged-and-decayed CF steel specimens are then compared with the experimental data. Finally, conclusions are made.

2. TENSILE PROPERTIES OF 21-6-9 STAINLESS STEEL

The stress-strain relation for the arc-shaped tension specimens of uncharged CF 21-6-9 stainless steels was obtained from a tensile test with a round bar specimen in [3]. The Young's modulus E is determined to be 177.33 GPa and the Poisson's ratio ν is 0.3 for the uncharged CF 21-6-9 stainless steels. For the plastic part of the stress-strain relation, the initial part of the true stress-plastic strain curve is determined from the experimental engineering stress-strain curve before the onset of the load drop. For the true strain larger than the one corresponding to the maximum load, a power-law relation is used to extend the initial experimental curves as

$$\sigma = K(\varepsilon_p)^n \quad (1)$$

where σ is the true stress, ε_p is the plastic strain, and K and n are material constants selected to extend the experimental data to large plastic strains. The details of the tensile test modeling and the procedures to obtain the true stress-true plastic strain curve were presented in Wu et al. [3]. The material constants K of 1,770 MPa and n of 0.225 were selected in [3] to match the stress-strain relation from the experiment. The material constants for the uncharged CF steel are listed in Table 1. Figure 1 shows the true stress-true plastic strain curve as a black solid line of the uncharged CF steel based on the material constants described above.

The tensile stress-strain curve for the tritium-charged-and-decayed CF steel with the helium concentration of 253 appm (atomic parts per million), which matches that of the tritium-charged-and-decayed arc-shaped tension CF steel specimen, is not available. Therefore, an estimation procedure similar to that in [3] was used to estimate the stress-strain curve for the tritium-charged-and-decayed CF steel based on the yield stresses of the HERF steels [1]. The interpolation was carried out in terms of the helium concentration of the HERF steels with respect to the yield stress to obtain the plastic response of the tritium-charged-and-decayed CF steel. The interpolation procedure is summarized in Table 2. Here, two groups of uncharged HERF steels and tritium-charged-and-decayed HERF steels with the helium concentration of 390 appm as reported in [1] were selected as the reference steels for the interpolation procedure. The uncharged steel A and the tritium-charged-and-decayed steel A have the low yield stresses of 825 MPa and 882 MPa, respectively. The uncharged steel B and the tritium-charged-and-decayed steel B have the high yield stresses of 918 MPa and 1,013 MPa, respectively. Based on the helium concentration, the linearly interpolated yield stresses of the tritium-charged-and-decayed A and B steels with the helium concentration of 253 appm are 862 MPa and 980 MPa, respectively. For the target uncharged steel with the yield stress of 856 MPa and for the target tritium-charged-and-decayed steel with the helium concentration of 253 appm, the linearly interpolated yield stress of the target tritium-charged-and-decayed steel is 901 MPa. With the assumption that the effects of the helium concentration on the increase of the yield stress for both the CF and HERF steels are similar, the yield stress for the tritium-charged-and-decayed CF steel with the helium concentration of 253 appm is assumed to be 901 MPa of the target HERF steel. The true stress-true plastic strain of the tritium-charged-and-decayed CF steel is then scaled up from the uncharged one by the larger yield stress of 901 MPa. The resulting tensile properties with σ_Y = 901.22 MPa, K = 1,863 MPa, and n = 0.225 for the tritium-charged-and-decayed CF steel with the helium concentration of 253 appm are listed in Table 1. The estimated tensile true stress-true plastic strain curve shown as the dashed line for the tritium-charged-and-decayed CF steel is about 5.2% higher than the uncharged one shown as the solid line in Figure 1. For the finite element simulation of the crack extension in the arc-shaped tension specimen of the tritium-charged-and-decayed CF steel, the estimated true stress-true plastic strain curve for the tritium-charged-and-decayed CF steel shown in Figure 1 will be used.

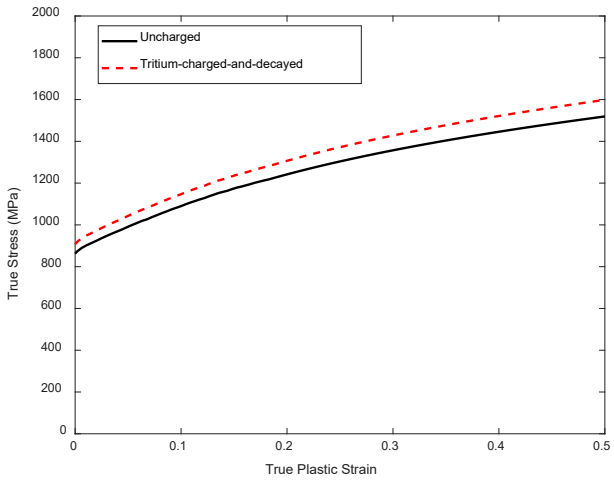

Figure 1: The true stress-true plastic strain curves for the uncharged and tritium-charged-and-decayed CF steels.

Table 1: The material constants for the uncharged and tritium-charged-and-decayed CF 21-6-9 steels.

Specimen	E (GPa)	ν	σ_Y (MPa)	K (MPa)	n
Uncharged	177.33	0.3	856.48	1,770	0.225
Tritium-charged-and-decayed	177.33	0.3	901.22	1,863	0.225

Table 2: Experimental and interpolated yield stresses for the uncharged and tritium-charged-and-decayed HERF steels.

Steel	Yield stress (MPa) from experiment for helium concentration of 0 appm	Yield stress (MPa) from interpolation for helium concentration of 253 appm	Yield stress (MPa) from experiment for helium concentration of 390 appm
A	825	862 (interpolated)	882
Target	856	901 (estimated)	
B	918	980 (interpolated)	1,013

3. FRACTURE TESTS

Arc-shaped tension specimens were made and tested [2]. An arc-shaped tension specimen is schematically shown in Figure 2. The specimens were fatigue-cracked before the fracture tests. The crack lengths with consideration of the fatigue pre-crack lengths are 4.95 mm for the uncharged CF steel specimen and 4.32 mm for the tritium-charged-and-decayed CF steel specimen, respectively. The tritium-charged-and-decayed arc-shaped tension specimens were prepared by exposing the pre-cracked specimens to tritium gas at 34 MPa at 350°C for seven years. The helium concentration of the specimen was measured to be 253 appm as mentioned earlier. Both the uncharged (as-received) and tritium-charged-and-decayed arc-shaped tension specimens were tested.

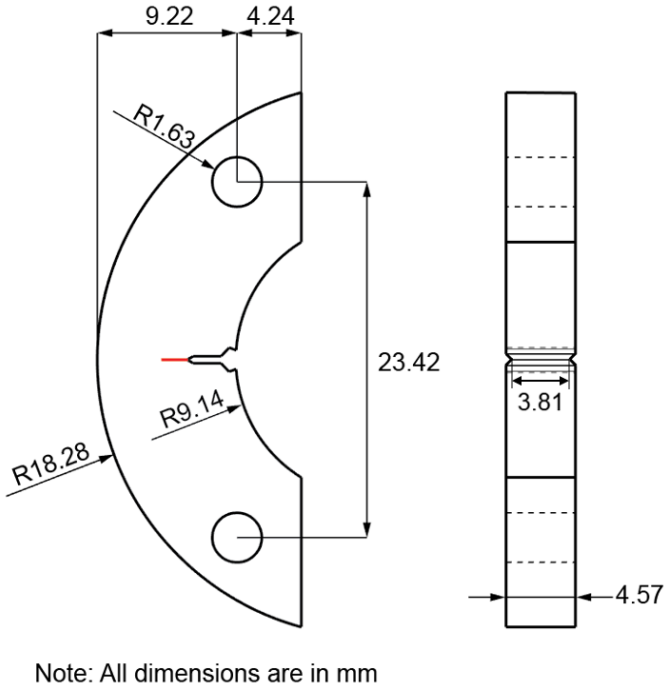

Figure 2: A schematic of an arc-shaped tension specimen.

The fracture tests [2] were conducted at room temperature in air using a screw-driven testing machine with a crosshead speed of 0.002 mm/s. The load, load-line displacement (using a gage clipped to the crack mouth), and crack length were recorded during the tests. The crack length was monitored using an alternating direct current potential drop system following the guidelines provided in ASTM E647 [8]. The J-integral vs. crack extension (J vs. Δa) curves were developed from the data using ASTM E1820 [9]. The J-R curves for the arc-shaped tension specimens of the uncharged (Specimen No. H94-4) and the tritium-charged-and-decayed (Specimen No. H94-72) CF 21-6-9 steels are shown in Figure 3. It should be noted that the stress-strain curve for the uncharged CF steel and the estimated stress-strain curve for the tritium-charged-and-decayed CF steel are very close as shown in Figure 1, but the J-R curves obtained from the arc-shaped tension specimens are significantly different as shown in Figure 3.

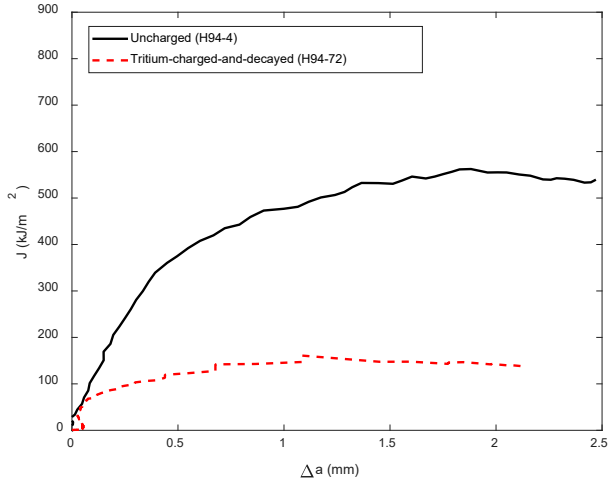

Figure 3: The J-integral vs. crack extension (J-R) curves for the uncharged and tritium-charged-and-decayed CF steel specimens.

4. TWO-DIMENSIONAL (2-D) PLANE STRAIN MODELING OF FRACTURE TESTS

4.1 Finite Element Model

The geometry of the 2-D finite element models follows the geometry of the arc-shaped tension specimen shown in Figure 2. The crack lengths including the fatigue pre-crack lengths are 4.95 mm and 4.32 mm, respectively, for the uncharged specimen (H94-4) and the tritium-charged-and-decayed specimen (H94-72). The specimen thickness is 4.57 mm for the as-received and tritium-charged-and-decayed specimens. The net section thickness is 3.81 mm without counting side grooves. The true stress-true plastic strain curves for the uncharged steel (solid line) and the tritium-charged-and-decayed steel (dashed line) shown in Figure 1 are used in the fracture test simulations.

Figure 4(a) shows the 2-D finite element model of the arc-shaped tension specimen of the uncharged steel in a Cartesian $X-Y$ coordinate system, and Figure 4(b) shows a closeup view near the crack tip. As shown in Figure 4(a), rigid links are placed from two reference points at the centers of the two pin holes to the surface nodes of the two pin holes. The two reference points

are used as the control points. For the boundary conditions, an upward displacement in the *Y* direction is applied at the upper control point. The displacement in the *X* direction at the upper control point is constrained. The displacements in the *X* and *Y* directions at the lower control point are fixed. Since the region near the mounting notches hardly deforms, the detailed design of the notches for mounting the clip gauge is not modeled. The locations to take the crack mouth opening displacements are marked as red dots in Figure 4(b). The 2-D finite element model of the arc-shaped tension specimen of the tritium-charged-and-decayed steel is quite similar and will not be shown. Plane strain linear elements with full integration (CPE4) are used to model the arc-shaped tension specimen. The smallest elements of 0.05 mm by 0.05 mm are located near the crack and the ligament. Other element sizes are from 0.1 mm by 0.1mm to 0.4 mm by 0.4 mm. The PPR user-defined cohesive element subroutine [10, 11] for ABAQUS is adopted here but with a smooth trapezoidal traction-separation law. The cohesive elements are placed along the crack line ahead of the crack tip in the -*X* direction. All cohesive elements have the same element size of 0.05 mm.

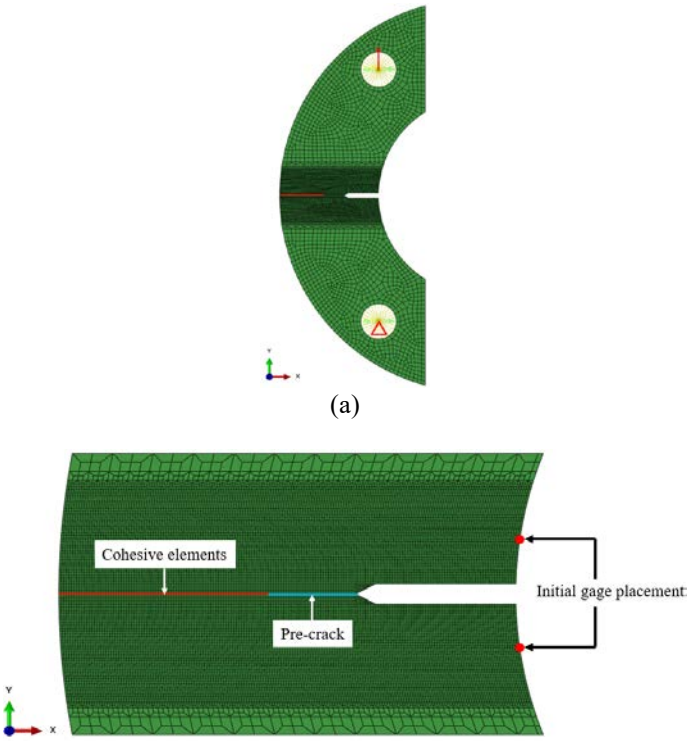

Figure 4: (a) The finite element model of the arc-shaped tension specimen of the uncharged CF 21-6-9 steel and (b) a closeup view of the refined mesh near the crack tip with the cohesive elements along the crack line.

4.2 Cohesive Zone Model

Trapezoidal traction-separation laws [4-7] were usually used to characterize the crack extensions in ductile metals. Figure 5 shows a schematic of the normalized smooth trapezoidal traction-separation law [6] used in this study. The smooth trapezoidal traction-separation law consists of three polynomials as

$$T = \begin{cases} T_0\left[2\left(\dfrac{\delta}{\delta_1}\right)-\left(\dfrac{\delta}{\delta_1}\right)^2\right] & 0 \le \delta < \delta_1 \\ T_0 & \delta_1 \le \delta < \delta_2 \\ T_0\left[2\left(\dfrac{\delta-\delta_2}{\delta_0-\delta_2}\right)^3-3\left(\dfrac{\delta-\delta_2}{\delta_0-\delta_2}\right)^2+1\right] & \delta_2 \le \delta < \delta_0 \end{cases} \quad (2)$$

where T is the traction and T_0 is the cohesive strength. The separation is represented by δ. The separation at the end of the initial part of the traction-separation law is represented by δ_1. The separation at the onset of softening is represented by δ_2. The final separation is represented by δ_0 when the traction becomes zero. The cohesive energy Γ is defined as the area under the traction-separation curve. It should be noted that δ_1 should be small enough to prevent inducing too much artificial compliance but large enough to assure computational stability. In this study, the ratio δ_1/δ_0 is selected to be 0.008 for all simulations. The softening ratio δ_2/δ_0 usually has a minor influence on the simulation results so that the softening ratio δ_2/δ_0 is chosen to be a constant of 0.3 for all simulations.

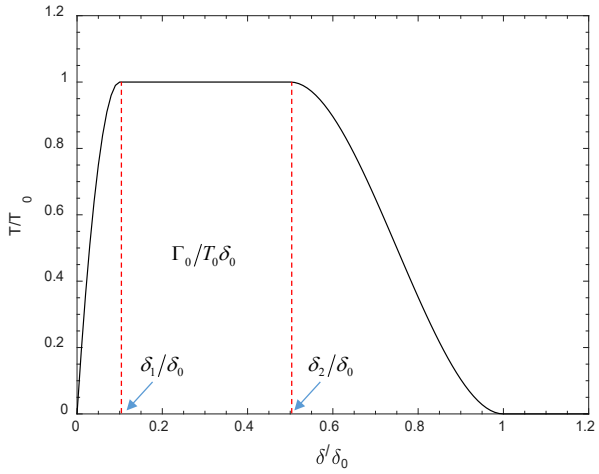

Figure 5: A schematic of a normalized smooth trapezoidal traction-separation law.

4.3 Selection of cohesive parameters

In order to select the cohesive strength and cohesive energy for the simulations of fracture tests for the uncharged and tritium-charged-and-decayed specimens, the corresponding finite element models without cohesive elements but with the same geometries and meshes similar to those shown in Figures 4(a) and 4(b) for the uncharged and tritium-charged-and-decayed specimens are adopted. Figure 6(a) shows a comparison of the

experimental and computational load-displacement curves of the finite element model without cohesive elements for the uncharged specimen (H94-4). The deviation load P_{dev} is defined as the load at which the computational load-displacement curve (red dashed line) deviates from the experimental load-displacement curve (black solid line). The deviation load P_{dev} of 2,070 N of the uncharged specimen (H94-4) is marked in Figure 6(a). The J integral at the deviation load, J_{dev} = 33.9 kJ/m^2, is determined from the experimental data. The deviation load P_{dev} and the J integral at the deviation load J_{dev} for the uncharged specimen are listed in Table 3. Figure 6(b) shows a comparison of the experimental and computational load-displacement curves of the finite element model without cohesive elements for the tritium-charged-and-decayed specimen (H94-72). The deviation load P_{dev} of 3,558 N of the tritium-charged-and-decayed specimen (H94-72) is marked in Figure 6(b). The J integral at the deviation load, J_{dev} = 27.8 kJ/m^2, is determined from the experimental data. The deviation load P_{dev} and the J integral at the deviation load J_{dev} for the tritium-charged-and-decayed specimen are listed in Table 3.

Figure 7(a) shows the distribution of the opening stress ahead of the initial crack tip at the deviation load for the uncharged specimen (H94-4). The maximum value of the distribution of the opening stress ahead of the initial crack tip at the deviation load is 2,720 MPa. Figure 7(b) shows the distribution of the opening stress ahead of the initial crack tip at the deviation load for the tritium-charged-and-decayed specimen (H94-72). The maximum value of the distribution of the opening stress ahead of the initial crack tip at the deviation load is 2,850 MPa.

The J integrals at the deviation loads of the arc-shaped tension specimens are taken as the reference cohesive energies for the uncharged and tritium-charged-and-decayed specimens. The maximum values of the distributions of the opening stresses ahead of the initial crack tips in the arc-shaped tension specimens are taken as the reference cohesive strengths for the uncharged and tritium-charged-and-decayed specimens. The cohesive strengths and cohesive energies are then adjusted as fixed values to match the maximum loads of the experimental load-displacement curves of the arc-shaped tension specimens. The selected cohesive strengths and cohesive energies for uncharged and tritium-charged-and-decayed specimens are listed in Table 4. Figure 8 shows the identified smooth trapezoidal traction-separation laws for the uncharged and tritium-charged-and-decayed CF 21-6-9 austenitic stainless steel specimens.

Table 3: Experimental data corresponding to the deviation loads of fracture tests.

Specimen	P_{dev} (N)	J_{dev} (kJ/m^2)
Uncharged	2,070	33.9
Tritium-charged-and-decayed	3,558	27.8

Table 4: The cohesive parameters for the smooth trapezoidal traction-separation law.

Specimen	σ_{max} (MPa)	Γ (kJ/m^2)	δ_0 (μm)
Uncharged	2,760	40.0	22.5
Tritium-charged-and-decayed	2,840	20.0	11.0

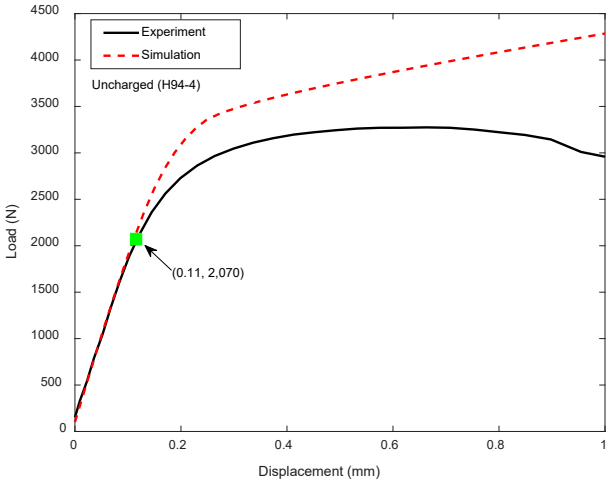

(a)

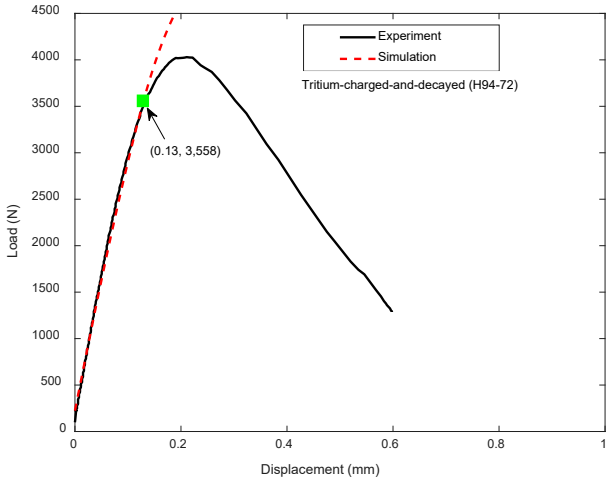

(b)

Figure 6: Comparison of the computational and experimental load-displacement curves of the finite element models without cohesive elements for the (a) uncharged (H94-4) and (b) tritium-charged-and-decayed (H94-72) specimens.

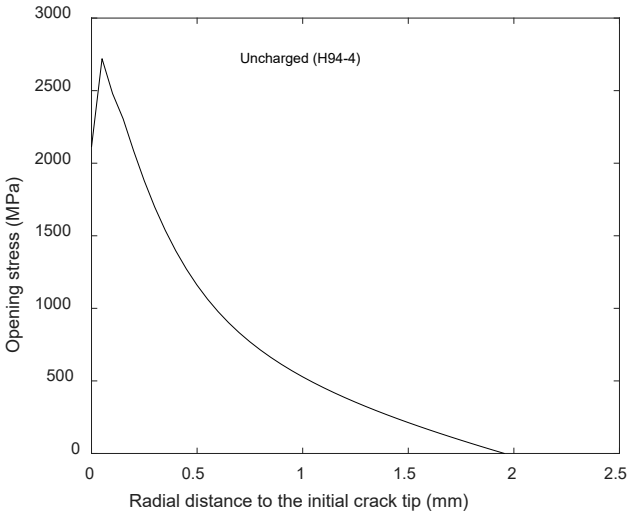

(a)

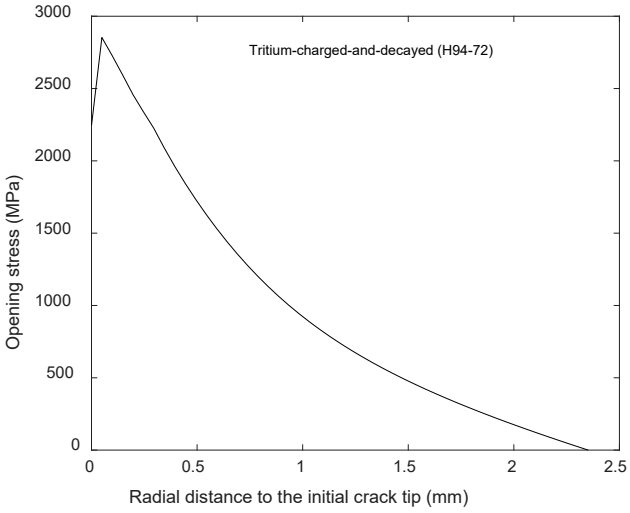

(b)

Figure 7: The distributions of the opening stresses ahead of the initial crack tips at the deviation loads for the (a) uncharged (H94-4) and (b) tritium-charged-and-decayed (H94-72) specimens.

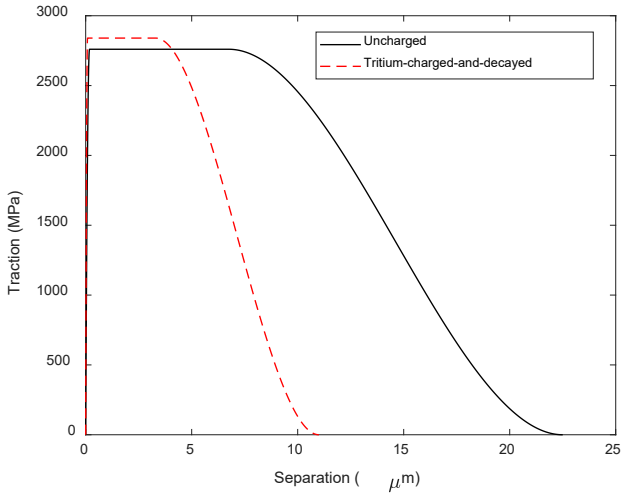

Figure 8: The smooth trapezoidal traction-separation laws for the uncharged and tritium-charged-and-decayed CF steel specimens.

4.4 Computational Results

The experimental and computational load-displacement, load-crack extension, crack extension-displacement, and J-R curves for the uncharged specimen are shown in Figures 9(a) to 9(d), respectively. Because the cohesive strength T_0 of 2,760 MPa and cohesive energy Γ of 40 kJ/m^2 are selected to fit the maximum load of the load-displacement data, the computational curve shown in Figure 9(a) agrees reasonably well with the experimental data. However, the computational displacement corresponding to the maximum load in the load-displacement curve is smaller than the experiment data. The crack initiation load of 2,621 N corresponding to the crack initiation with cohesive elements is also marked in Figure 9(a). The computational load-crack extension curve in Figure 9(b) generally agrees with the experiment data. However, the computational crack extension-displacement curve shows some discrepancy from the experimental data in Figure 9(c) due to the early drop of the load in the computational load-displacement curve as shown in Figure 9(a). The computational J-R curve is in good agreement with the experiment data as shown in Figure 9(d). In Figure 9(d), the red dashed line is the computational J-R curve based on the ASTM E1820 standard [9] by using the computational load-displacement, load-crack extension, and crack extension-displacement curves as shown in Figures 9(a) to 9(c).

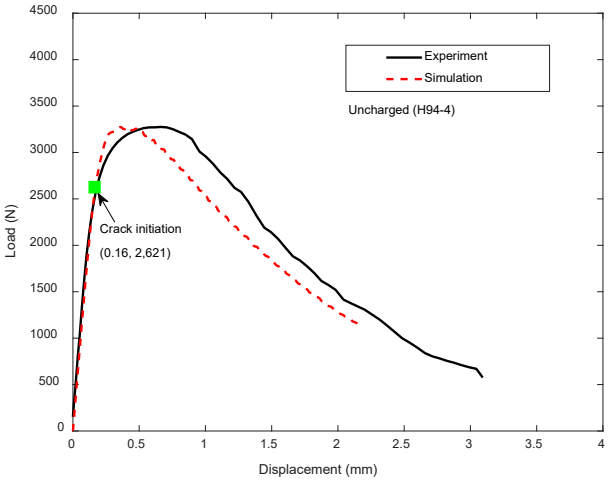

(a)

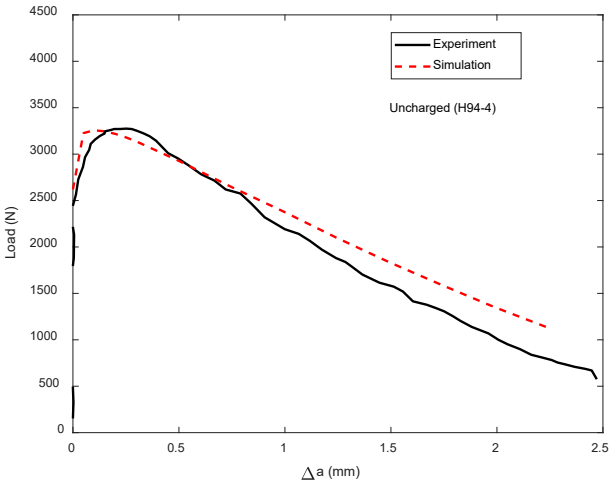

(b)

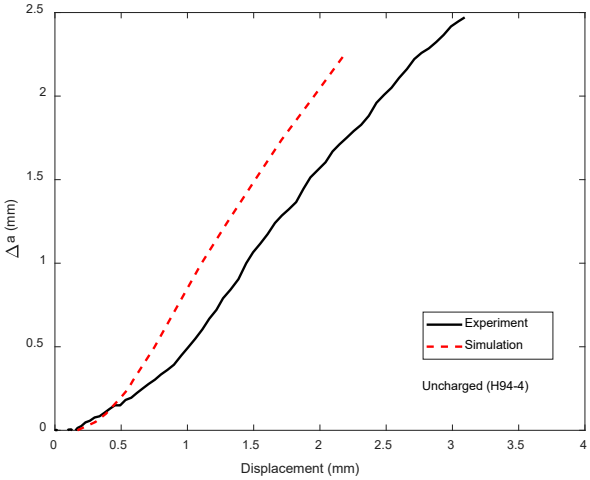

(c)

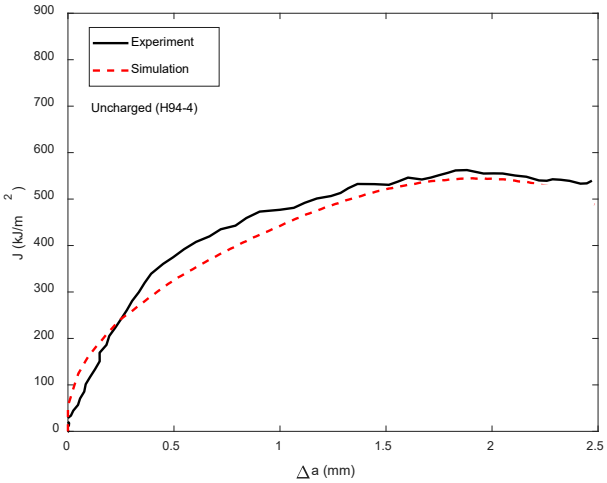

(d)

Figure 9: Comparisons of the experimental and computational results for the uncharged specimen: (a) load-displacement curves, (b) load-crack extension curves, (c) crack extension-displacement curves, and (d) J-R curves.

For the tritium-charged-and-decayed specimen, the experimental and computational load-displacement, load-crack extension, and crack extension-displacement, and J-R curves are shown in Figures 10(a) to 10(d), respectively. The computational load-displacement curve in Figure 10(a) agrees well with the experimental data with the cohesive strength T_0 of 2,840 MPa and cohesive energy Γ of 20 kJ/m^2 selected to fit the maximum load of the load-displacement data of the tritium-charged-and-decayed specimen. The crack initiation load of 2,774 N corresponding to the crack initiation with cohesive elements is also marked in Figure 10(a). The computational load-crack extension, crack extension-displacement, and J-R curves shown in Figures 10(b) to 10(d) are also in good agreement with the experimental data.

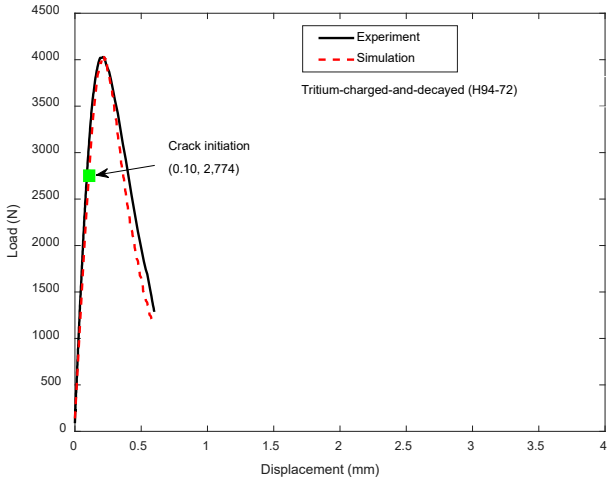

(a)

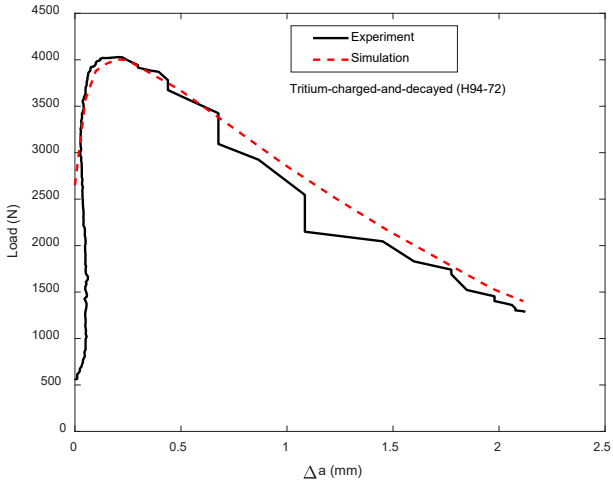

(b)

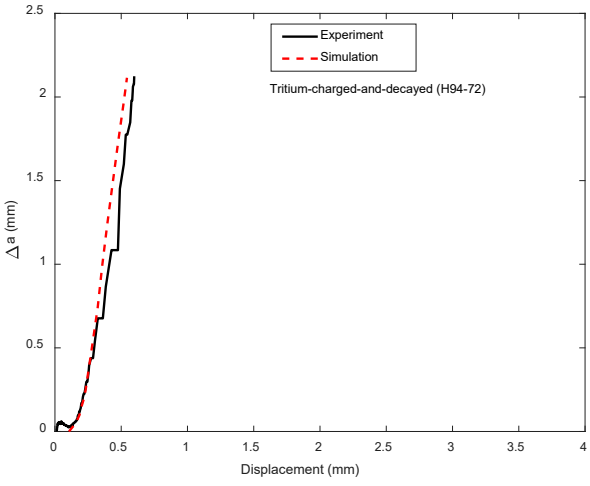

(c)

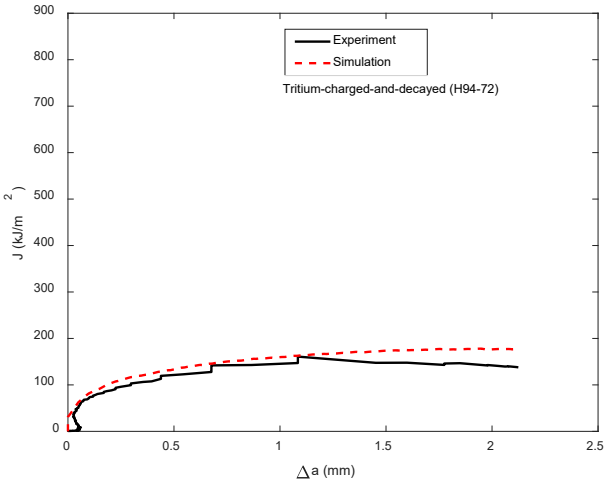

(d)

Figure 10: Comparisons of the experimental and computational results for the tritium-charged-and-decayed specimen: (a) load-displacement curves, (b) load-crack extension curves, (c) crack extension-displacement curves, and (d) J-R curves.

5. CONCLUSIONS

Crack extensions in arc-shaped tension specimens of uncharged and tritium-charged-and-decayed conventionally forged (CF) 21-6-9 austenitic stainless steels are simulated by two-dimensional finite element analyses using the cohesive zone modeling (CZM) approach. The material constitutive relation is obtained from fitting the experimental tensile stress-strain data of a round bar specimen of the uncharged CF steel. The material constitutive relation for the tritium-charged-and-decayed CF steel is estimated based on the experimental tensile stress-strain data of the uncharged CF 21-6-9 austenitic stainless steel and the tritium-charged-and-decayed high-energy-rate-forged (HERF) 21-6-9 stainless steels. The cohesive zone model with the smooth trapezoidal traction-separation law is then adopted to simulate crack extensions in arc-shaped tension specimens of the uncharged and tritium-charged-and-decayed CF steels. The J integrals at the deviation loads of the arc-shaped tension specimens are taken as the reference cohesive energies and the maximum opening stresses ahead of the initial crack tips in the arc-shaped tension specimens are taken as the reference cohesive strengths for the uncharged and tritium-charged-and-decayed CF steel specimens. The cohesive strengths and cohesive energies are then adjusted to match the maximum loads of the experimental load-displacement curves of the arc-shaped tension specimens. The computational results showed that the computational load-displacement, load-crack extension, crack extension-displacement, and J-R curves of the uncharged and tritium-charged-and-decayed CF steel specimens are compared well with the experimental data.

ACKNOWLEDGEMENTS

The support of this research by the U.S. Department of Energy is appreciated. Helpful discussions with Dr. Shin-Jang Sung of University of Michigan are appreciated.

REFERENCES

[1] Morgan, Michael J. “The Effects of Hydrogen Isotopes and Helium on the Flow and Fracture Properties of 21-6-9 Stainless Steel.” *Proceedings of the Morris E. Fine Symposium*, *TMS*: pp. 105-111. Warrendale, PA, 1991.

[2] Morgan, Michael J. “Tritium Aging Effects on the Fracture Toughness Properties of Forged Stainless Steel.” *Materials Innovations in an Emerging Hydrogen Economy*. John Wiley & Sons, Inc, Hoboken (2008): pp. 221-235.

[3] Wu, Shengjia, Sung, Shin-Jang, Pan, Jwo, Lam, Poh-Sang, Morgan, Michael J. and Korinko, Paul S. “Modeling of Crack Extensions in Arc-Shaped Specimens of Hydrogen-Charged Austenitic Stainless Steels Using Cohesive Zone Model.” *Proceedings of the ASME 2018 Pressure Vessels & Piping Conference*: PVP2018-84919. Prague, Czech Republic, July 15-20, 2018.

[4] Tvergaard, Viggo and Hutchinson, John W. “The Relation between Crack Growth Resistance and Fracture Process Parameters in Elastic-Plastic Solids.” *Journal of the Mechanics and Physics of Solids* Vol. 40 No. 5 (1992): pp. 1377-1397.

[5] Tvergaard, Viggo and Hutchinson, John W. “Effect of Strain-Dependent Cohesive Zone Model on Predictions of Crack Growth Resistance.” *International Journal of Solids and Structures* Vol. 33 No. 20–22 (1996): pp. 3297–3308.

[6] Cornec, Alfred, Scheider, Ingo and Schwalbe, Karl-Heinz. “On the Practical Application of the Cohesive Model.” *Engineering Fracture Mechanics* Vol. 70 No. 14 (2003): pp. 1963-1987.

[7] Wu, Shengjia, Sung, Shin-Jang, Pan, Jwo, Lam, Poh-Sang and Scarth, Douglas A. “Crack Extensions in Compact Tension Specimens of Hydrided Irradiated Zr-2.5Nb Materials Using Cohesive Zone Model.” *Proceedings of the ASME 2017 Pressure Vessels & Piping Conference*: PVP2017-65022. Waikoloa, Hawaii, USA, July 16-20, 2017.

[8] ASTM E647-95a. *Standard Test Method for Measurement of Fatigue Crack Growth Rates.* ASTM International, West Conshohocken (1996).

[9] ASTM E1820-99. *Standard Test Method for Measurement of Fracture Toughness*. ASTM International, West Conshohocken (1999).

[10] Park, Kyoungsoo, Paulino, Glaucio H. and Roesler, Jeffery R. “A Unified Potential-Based Cohesive Model of Mixed-Mode Fracture.” *Journal of the Mechanics and Physics of Solids* Vol. 57 No. 6 (2009): pp. 891–908.

[11] Park, Kyoungsoo and Paulino, Glaucio H. “Computational Implementation of the PPR Potential-Based Cohesive Model in ABAQUS: Educational Perspective.” *Engineering Fracture Mechanics* Vol. 93 (2012): pp. 239-262.